J. Fluid Mech. (1981), *vol.* 103, *pp.* 297–320
Printed in Great Britain

A quasi-linear theory for rotating flow over topography. Part 2. Beta-plane annulus

By MICHAEL K. DAVEY†

The Joint Institute for the Study of the Atmosphere and Ocean,
University of Washington, Seattle, Washington 98195 U.S.A.

(Received 16 July 1979 and in revised form 25 March 1980)

An obstacle in westerly flow on a periodic β-plane can generate resonant Rossby waves and cause large perturbations to the flow field. The pattern and strength of the flow can vary markedly in response to relatively small changes in the forces driving the system. The aim of this paper is to develop a simple theory valid in these circumstances. Such a theory has application to the dynamics of planetary scale quasi-steady perturbations in the atmosphere.

A series of models for barotropic quasi-geostrophic flow in an annulus is presented. An implicit quasi-linear model, with zonally averaged flow parametrized in terms of topography shape and net zonal mass transport, gives good agreement with nonlinear calculations. In one case stable multiple equilibria are predicted and confirmed, but the multiplicity regime is small.

1. Introduction

This is the second part of an investigation of topographic effects on periodic quasi-geostrophic flow. The aim is to model the feedback between zonally averaged flow and wave-topography interactions, and hence accurately describe the response of the system to a particular driving force. By finding the response for a range of forces the effect of variations in the driving can be deduced. This has important application to the dynamics of large-scale flow perturbations in the atmosphere, which are almost stationary when averaged over several days. These patterns sometimes change from one quasi-steady configuration to another, for reasons that are not well understood. Charney & DeVore (1979) suggest that internal fluctuations can trigger changes from one stable equilibrium to an alternative state. Along similar lines Hart (1979) has presented a theory involving multiple branches with a hysteresis effect as external forces vary.

In part 1 (Davey 1980) a quasi-linear theory was developed to explain large responses to small forcing changes in terms of positive feedback between zonal flow, resonant Rossby waves, and topography in a β-plane channel. Multiple steady states for fixed external parameters were found, but the inclusion of several waves and modification of the zonal flow profile severely reduced the multiple solution regime. Part 2 is an extension of that theory to annular geometry, to include the angular momentum budget relevant to motion on the surface of a sphere. Another reason for applying the

† Now at Department of Applied Mathematics and Theoretical Physics, University of Cambridge, Silver Street, Cambridge, England.

0022–1120/81/4678–3380 $02.00

theory to an annulus is that these results can be more readily checked by laboratory experiment than those from the channel theory.

Rossby waves in a rotating annulus with a free surface (but flat bottom topography) were investigated by Phillips (1965). The theoretical dispersion relation was verified by experiments with an oscillating paddle used to excite different frequencies. Close agreement with the dispersion relation for a β-plane channel (Haurwitz 1940*a*) was also found. No resonance effects occurred because the waves generated damped out before travelling around the annulus. Holton (1971) has also studied Rossby waves in a β-plane annulus. A travelling source-sink system was used in experiments to specifically excite resonant waves with various zonal wavenumbers. There was qualitative agreement with β-plane channel theory.

With regard to topographic effects, an interesting series of experiments using a rotating hemisphere has been described by Fultz & Long (1951), Long (1952), Fultz & Frenzen (1955) and Frenzen (1955). Westerly flow relative to an obstacle generated planetary waves with wavenumber depending on the relative angular speeds of the basic flow and the obstacle. The results are mainly descriptive, though the dispersion relation for Rossby–Haurwitz waves on a sphere (Haurwitz 1940*b*) was verified. A variety of obstacles was used, ranging from cylinders extending through the entire depth of the apparatus, to equator–pole ridges of fractional height. Varying the latitude of an obstacle showed that wave patterns were weaker at higher latitudes. In the associated theoretical work friction effects and topographic drag were not considered, but only qualitative comparison with the experiments was sought. The quasi-linear theory presented in the following sections takes these effects into account.

As in part 1 an implicit method with the zonally averaged flow parametrized in terms of the net circumpolar transport Q is used. Quasi-linear equations for the wave structure are then obtained, and these waves are in turn related to Q. The validity of the approximations involved is determined by comparing quasi-linear results with numerical solutions of the nonlinear quasi-geostrophic vorticity equation.

The basic equations needed are given in the next section. The simplest implicit theory is described in § 3 with analytic and numerical results. The nonlinear calculations in § 4 suggest a better parameterization, and the improved implicit theory used in §§ 5 and 6 gives good agreement for a range of conditions. Multiple solutions are found when the latitude range is relatively large. In several cases unsteady nonlinear solutions are obtained instead of predicted multiple steady states. Application to the atmosphere and ocean is discussed in § 7.

2. Quasi-geostrophic equations

Cylindrical polar co-ordinates will be used for the annular geometry shown in figure 1. Non-dimensional variables are defined by

$$r = r^*/r_1^*, \quad z = z^*/H_0^*, \quad (u, v) = (u^*, v^*)/C^*, \quad t = \omega t^* f_A^*,$$

where asterisks denote dimensional terms. The vertical scale H_0^* is the average depth of the fluid, and the horizontal length scale is the inner radius r_1^*. The horizontal velocity $\mathbf{u}^* = (u^*, v^*)$ is relative to a reference frame rotating with angular velocity $\frac{1}{2}f_A^*$. A rigid upper lid with relative angular velocity $\pm 2\Omega_0^*$ is used to drive the system, so a velocity scale $C^* = r_1^* \Omega_0^*$ is appropriate.

The annular geometry can be regarded as an approximation to a region bounded by two latitude circles on a sphere. The β-plane approximation for the variation of effective Coriolis force with latitude is

$$f^* = f_A^* - \beta^*(r^* - r_A^*),$$

where $r_A^* = \frac{1}{2}(r_1^* + r_2^*)$. In non-dimensional form

$$f = f^*/f_A^* = 1 - \beta(r - r_A), \tag{2.1}$$

where $\beta = \beta^* r_1^*/f_A^*$. (Further details are given in appendix C.)

Other important non-dimensional parameters are the Rossby number

$$\epsilon = C^*/f_A^* r_1^* = \Omega_0^*/f_A,$$

and the Ekman number $E = 2\nu/f_A^* H_0^{*2}$. (ν is a vertical eddy viscosity.) These express respectively the ratio of inertial and viscous forces to the Coriolis force. The bottom topography is $h = h_0 S(r, \theta)$, with non-dimensional height scale $h_0 = h_0^*/H_0^*$ and shape $S(r, \theta)$.

For slow large-scale flow over shallow obstacles the parameters ω, ϵ, $E^{\frac{1}{2}}$, β and h_0 are small (less than unity). Away from thin boundary layers the flow is almost geostrophic and independent of z, and to a good approximation is governed by the quasi-geostrophic vorticity equation. This is

$$\omega\zeta_t + \mathbf{u} \cdot \nabla(\epsilon\zeta + h - \beta r) + E^{\frac{1}{2}}\zeta = \tfrac{1}{2}E^{\frac{1}{2}}\zeta_T \tag{2.2}$$

where ζ and ζ_T are the internal and upper surface vertical vorticity components. The horizontal flow is non-divergent to this order of approximation, so a stream function $\psi(r, \theta)$ can be defined by

$$u = -\psi_\theta/r, \quad v = \psi_r. \tag{2.3}$$

(For geostrophic flow ψ is equivalent to a non-dimensional pressure field.) In terms of ψ, (2.2) becomes

$$\omega\nabla^2\psi_t + J(\psi, \epsilon\nabla^2\psi + h - \beta r) + E^{\frac{1}{2}}\nabla^2\psi = 2E^{\frac{1}{2}}\Omega_0, \tag{2.4}$$

where J is the Jacobian operator

$$J(\psi, \chi) = (\psi_r \chi_\theta - \psi_\theta \chi_r)/r,$$

and $\zeta_T = 4\Omega_0$ for rigid-lid driving has been used. ($\Omega_0 = \pm 1$ will be used to force westerly and easterly flow.)

The side walls are streamlines, so boundary conditions are

$$\psi(r_1, \theta, t) = 0, \quad \psi(r_2, \theta, t) = Q(t), \tag{2.5}$$

where Q is the net zonal mass transport

$$Q(t) = \int_{r_1}^{r_2} v\, dr. \tag{2.6}$$

The system of equations is closed by the circulation condition

$$\oint (\omega\mathbf{u}_t + E^{\frac{1}{2}}\mathbf{u} - \tfrac{1}{2}E^{\frac{1}{2}}\mathbf{u}_T) \cdot \mathbf{dl} = 0, \tag{2.7}$$

as in part 1. (Note that there is some redundancy in the non-dimensional parameters. If ω, ϵ, β, $E^{\frac{1}{2}}$, h_0 are all multiplied by the same constant the system is unchanged.)

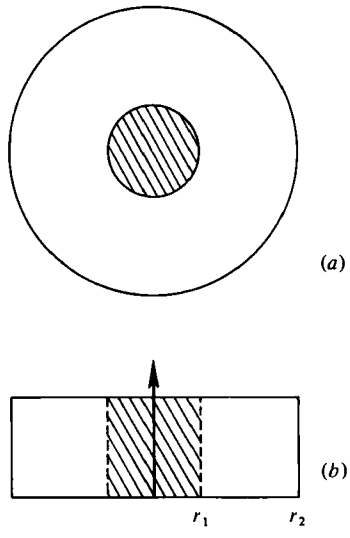

FIGURE 1. The annulus geometry: (*a*) plan view, (*b*) side view.

It is convenient to treat the flow as the sum of a zonal average and eddies. We put

$$\psi = [\psi] + \phi,$$

where

$$[\psi] = \frac{1}{2\pi}\int_{-\pi}^{\pi} \psi \, d\theta.$$

(Square brackets will indicate a zonal average.) From (2.5) boundary conditions for these components are

$$\begin{aligned} &\phi(r_1, \theta, t) = \phi(r_2, \theta, t) = [\psi(r_1, t)] = 0, \\ &[\psi(r_2, t)] = Q. \end{aligned} \tag{2.8}$$

The zonally averaged vorticity equation is

$$\omega[\zeta]_t + [J(\phi, \epsilon\nabla^2\phi + h)] + E^{\frac{1}{2}}[\zeta] = 2E^{\frac{1}{2}}\Omega_0. \tag{2.9}$$

Rearranging (2.9) and integrating using (2.7) at side walls gives the zonal average angular momentum equation

$$\omega[rv]_t + [\phi(\epsilon\nabla^2\phi + h)_\theta] + E^{\frac{1}{2}}[rv] = E^{\frac{1}{2}}rv_0, \tag{2.10}$$

where $v_0 = \Omega_0 r$. The eddy term in (2.10) is the sum of a radial eddy vorticity flux

$$[\text{flux}] = \epsilon[\phi\nabla^2\phi_\theta] = \epsilon[ur\nabla^2\phi] = \epsilon[u(rv)_r] \tag{2.11}$$

(equivalent to radial angular momentum advection), and a topographic drag

$$[\text{drag}] = [\phi h_\theta] = [ruh].$$

Dividing by r and integrating (2.10) gives

$$\omega Q_t + \int_{r_1}^{r_2} r^{-1}([\text{flux}] + [\text{drag}])\, dr + E^{\frac{1}{2}}Q = E^{\frac{1}{2}}Q_0, \tag{2.12}$$

where $Q_0 = \int_{r_1}^{r_2} v_0 \, dr$. In contrast to (2.15) in part 1, there is a contribution from eddy–

eddy interaction as well as eddy–topography interaction. The flux term appears because rearrangement of angular momentum can change Q, whereas rearrangement of linear momentum in the channel does not alter the net transport.

If (2.10) is multiplied by r and integrated, then a moment equation

$$\omega M_t + \int_{r_1}^{r_2} r[\text{drag}]\,dr + E^{\frac{1}{2}} M = E^{\frac{1}{2}} M_0 \tag{2.13}$$

is obtained, where

$$M = \int_{r_1}^{r_2} r^2 v\,dr, \quad M_0 = \int_{r_1}^{r_2} r^2 v_0\,dr.$$

This M-equation (as it will be called) has the advantage of having no nonlinear flux term. However, Q is needed for the boundary conditions on $[\psi]$ and Q cannot be recovered directly from M, so in general (2.13) cannot be used as an alternative to the Q-equation (2.12). (In later sections $[v]$ is parametrized and Q can then be found from M. The merits of (2.13) as a replacement for (2.12) in that context are discussed in § 5.)

From (2.4) the eddy vorticity equation is

$$\begin{aligned}\omega\nabla^2\phi_t + [v]\,(\epsilon\nabla^2\phi + h)_\theta/r + u[\epsilon\zeta + h - \beta r]_r \\ + J(\phi, \epsilon\nabla^2\phi + h) - [J(\phi, \epsilon\nabla^2\phi + h)] + E^{\frac{1}{2}}\nabla^2\phi = 0.\end{aligned} \tag{2.14}$$

The kinetic energy equation is

$$\tfrac{1}{2}\omega KE_t + E^{\frac{1}{2}} KE = E^{\frac{1}{2}}\pi \int_{r_1}^{r_2} v_0[v]\,r\,dr, \tag{2.15}$$

where

$$KE = \frac{1}{2}\int_{-\pi}^{\pi}\int_{r_1}^{r_2} (u^2 + v^2)\,r\,dr\,d\theta.$$

Rearranging (2.15) gives

$$\begin{aligned}\omega KE_t + E^{\frac{1}{2}} KE = E^{\frac{1}{2}} KE_0 - E^{\frac{1}{2}}\pi \int_{r_1}^{r_2} [v_0 - v]^2\,r\,dr \\ - \tfrac{1}{2}E^{\frac{1}{2}}\int_{-\pi}^{\pi}\int_{r_1}^{r_2} (\phi_r^2 + \phi_\theta^2/r^2)\,r\,dr\,d\theta,\end{aligned} \tag{2.16}$$

where

$$KE_0 = \pi\int_{r_1}^{r_2} v_0^2\,r\,dr.$$

Equation (2.16) shows that in a steady (or statistically steady) state the KE (or time average KE) is decreased by any disturbance to the uniform flow v_0.

The nonlinear equations (2.9), (2.12) and (2.14) were solved numerically using the semi-spectral method described in appendix B. For the steady quasi-linear approximations discussed in following sections, the eddy–eddy and eddy–topography interactions are omitted from the eddy vorticity equation. (The conditions for which this approximation is valid are not obvious in advance, due to the possible presence of resonant Rossby waves. One aim of this paper is to compare approximate and fully nonlinear results to test the above assumptions.) The approximate steady equations are

$$[v]\,(\epsilon\nabla^2\phi + h)_\theta/r + u[\epsilon\zeta + h - \beta r]_r + E^{\frac{1}{2}}\nabla^2\phi = 0, \tag{2.17}$$

and

$$E^{\frac{1}{2}}[v] = E^{\frac{1}{2}} v_0 - [\phi(\epsilon\nabla^2\phi + h)_\theta]/r. \tag{2.18}$$

Note that (2.17) and (2.18) can be combined to give

$$[v]^2 = [v]v_0 + [\phi\nabla^2\phi], \tag{2.19}$$

a relation independent of the external parameters and the topography.

Solving these equations still requires considerable effort due to the different feedback between [flux], [drag] and $[v]$ at each latitude. Further simplification is gained by parametrizing $[v]$ in terms of Q. The eddy stream-function ϕ can then be obtained as a function of Q from (2.17). The Q-equation thus becomes an implicit equation for Q.

The simplest approximation is to ignore the feedback and put $[v] = v_0$. (This is equivalent to the perturbation method described in part 1, appendix B.) The simplest implicit theory described in the next section uses the profile

$$[v] = v_0 Q/Q_0 = \Omega r,$$

with $\Omega/\Omega_0 = Q/Q_0$.

3. The simplest implicit theory

When $[v]$ is approximated by the uniform zonal flow

$$[v] = \Omega r \tag{3.1}$$

the eddy vorticity equation (2.17) reduces to the quasi-linear equation

$$\Omega(\epsilon\nabla^2\phi + h)_\theta + \beta\phi_\theta/r + E^{\frac{1}{2}}\nabla^2\phi = 0. \tag{3.2}$$

Further, Q and M are related to Ω by

$$Q = \tfrac{1}{2}\Omega(r_2^2 - r_1^2), \quad M = \tfrac{1}{4}\Omega(r_2^4 - r_1^4).$$

Thus Q and M are directly related by

$$M = \tfrac{1}{2}(r_2^2 + r_1^2)\,Q.$$

Analytic results, analogous to the simplest implicit channel theory of part 1, are given first to define resonance conditions.

(a) *Analysis using orthogonal modes*

The topography is written as a Fourier–Bessel series

$$h = h_0 \frac{1}{r} \sum_m \sum_n R_{mn}(r)\,(f_{mn}\cos m\theta + g_{mn}\sin m\theta). \tag{3.3}$$

The radial modes R_{mn} are orthogonal eigenfunctions of

$$\frac{d}{dr}\left(r\frac{dR}{dr}\right) + (\lambda^2 - m^2/r)\,R = 0,$$

with $R(r_1) = R(r_2) = 0$. (These modes depend on the zonal wavenumber m, so a single radial mode cannot be used as in part 1. Further details are given in appendix A.) The eddy streamfunction is likewise expanded as

$$\phi = \Omega h_0 \Sigma\Sigma R_{mn}(a_{mn}\cos m\theta + b_{mn}\sin m\theta), \tag{3.4}$$

with corresponding vorticity

$$\nabla^2\phi = -\frac{1}{r}\Omega h_0 \Sigma\Sigma \lambda_{mn}^2 R_{mn}(a_{mn}\cos m\theta + b_{mn}\sin m\theta).$$

From (3.2) we find

$$a_{mn} = m\{m(\epsilon\Omega\lambda_{mn}^2 - \beta)f_{mn} + E^{\frac{1}{2}}\lambda_{mn}^2 g_{mn}\}/D_{mn},$$
$$b_{mn} = m\{m(\epsilon\Omega\lambda_{mn}^2 - \beta)g_{mn} - E^{\frac{1}{2}}\lambda_{mn}^2 f_{mn}\}/D_{mn},$$

where

$$D_{mn} = m^2(\epsilon\Omega\lambda_{mn}^2 - \beta)^2 + E\lambda_{mn}^4.$$

Large perturbations will occur if dissipation is small and $\epsilon\Omega\lambda_{mn}^2 \approx \beta$, i.e. if resonant Rossby waves are excited.

The Q-equation gives, using $Q/Q_0 = \Omega/\Omega_0$,

$$E^{\frac{1}{2}}(r_2^2 - r_1^2)\left(1 - \frac{\Omega}{\Omega_0}\right) = h_0^2 \frac{\Omega}{\Omega_0} \sum_m \sum_n \sum_j m\Big\{a_{mn}g_{mj} - b_{mn}f_{mj} + \epsilon\Omega_0 \frac{\Omega}{\Omega_0}\lambda_{mj}^2(b_{mn}a_{mj} - a_{mn}b_{mj})\Big\}\int_{r_1}^{r_2} r^{-2} R_{mj}R_{mn}\,dr. \quad (3.6)$$

From (3.5) a_{mn} and b_{mn} are functions of Ω/Ω_0, so (3.6) is an implicit equation for Ω/Ω_0. A simpler alternative to (3.6) can be found using the M-equation and $M/M_0 = \Omega/\Omega_0$:

$$\tfrac{1}{4}(r_2^4 - r_1^4)\left(1 - \frac{\Omega}{\Omega_0}\right) = h_0^2 \frac{\Omega}{\Omega_0} \sum_m \sum_n m^2\lambda_{mn}^2(f_{mn}^2 + g_{mn}^2)\int_{r_1}^{r_2} R_{mn}^2\,dr/D_{mn}. \quad (3.7)$$

Note that these equations for Ω/Ω_0 are not equivalent. Using (3.7) avoids the flux term altogether, whereas [flux] must be calculated in the nonlinear theory, so we expect (3.6) to be more accurate.

If only one radial mode, n say, appears for each m then the [flux] term vanishes in (3.6) leaving

$$(r_2^2 - r_1^2)\left(1 - \frac{\Omega}{\Omega_0}\right) = h_0^2 \frac{\Omega}{\Omega_0} \sum_m m^2\lambda_{mn}^2(f_{mn}^2 + g_{mn}^2)\int_{r_1}^{r_2} r^{-2}R_{mn}^2\,dr/D_{mn}. \quad (3.8)$$

This has the same structure as, but is still not equivalent to, (3.7). Both (3.7) and (3.8) have the same properties as the simplest implicit result in part 1. The β-effect increases Ω/Ω_0 for easterly flow and decreases it, with the possible appearance of several resonant peaks, for westerly flow. The dynamics can be similarly described as a balance of generation and relative advection of Rossby waves. As in part 1, there may be multiple solutions for Ω for given external parameters, but Ω is unique if the internal Rossby-number $\epsilon Q/Q_0$ is specified.

The use of orthogonal modes is instructive, but to obtain actual solutions it is more convenient to use a numerical semi-spectral model.

(*b*) *Numerical results*

For all calculations presented in this and subsequent sections the topography used has the form

$$h = h_0 P(r)\Sigma f_m \cos m\theta, \quad (3.9)$$

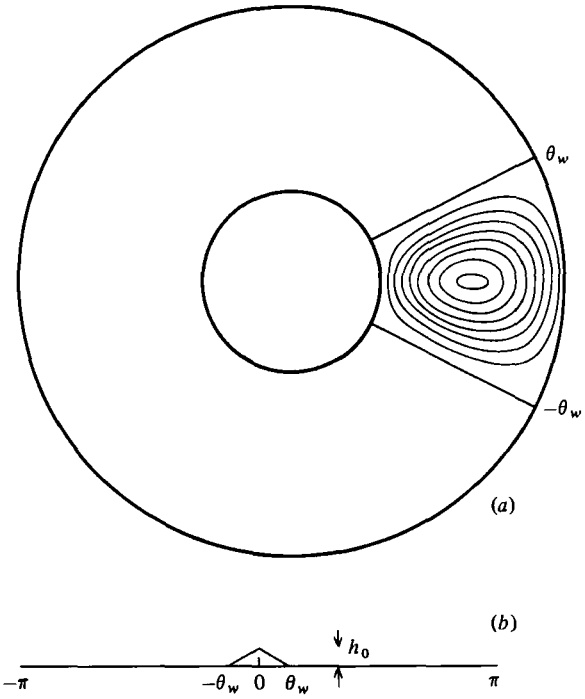

FIGURE 2. (*a*) Topography contours with $\theta_w = 0.5$. (*b*) Zonal profile at $r_A = \frac{1}{2}(r_1+r_2)$.

with radial profile

$$P(r) = \sin\pi\left(\frac{r-r_1}{r_2-r_1}\right).$$

A triangular zonal profile with angular half-width Q_w is represented by the Fourier series with

$$f_m = 2(1-\cos m\theta_w)/\pi\theta_w m^2.$$

(Topography contours are given in figure 2 for $\theta_w = 0{\cdot}5$ radians, $r_1 = 1$, $r_2 = 3$. Ten or more zonal wavenumbers were used in all calculations.)

The eddy stream function is written as

$$\phi = \mathrm{Re}\,\Sigma\, Z_m(r)\, e^{-\mathrm{i}m\theta}.$$

With the transform $r = r_2 e^{-y}$, (2.17) leads to the radial eddy structure equation

$$(\epsilon_m[v]/r + iE^{\frac{1}{2}})(Z_{yy} - m^2 Z) - r(\epsilon[\zeta]_r - \beta)\, mZ = -r[v]\, h_0 m f_m P(r). \tag{3.10}$$

When $[v] = \Omega r$ it is useful to put $Z = \Omega h_0 Y$ so (3.10) becomes

$$(\epsilon\Omega m + iE^{\frac{1}{2}})(Y_{yy} - m^2 Y) + r\beta m Y = -r^2 m f_m P. \tag{3.11}$$

The Q-equation gives

$$E^{\frac{1}{2}}(r_2^2 - r_1^2)\left(1 - \frac{\Omega}{\Omega_0}\right) = h_0^2 \frac{\Omega}{\Omega_0}\,\mathrm{Im}\sum_m m \int_{y_1}^{y_2} \overline{Y}(\epsilon\Omega Y_{yy} + f_m P)\, dy. \tag{3.12}$$

Equations (3.11) and (3.12) can be rapidly solved numerically to find Ω/Ω_0.

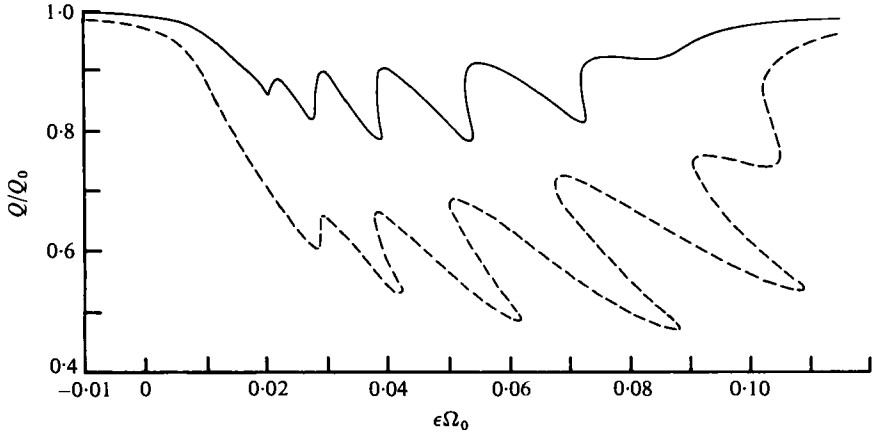

FIGURE 3. Dependence of Q/Q_0 on $\epsilon\Omega_0$, using the Q-equation with $[v] = \Omega r$, $\beta = 0{\cdot}4$, $E^{\frac{1}{2}} = 0{\cdot}01$, $h_0 = 0{\cdot}1$ (solid line), $h_0 = 0{\cdot}2$ (dashed line).

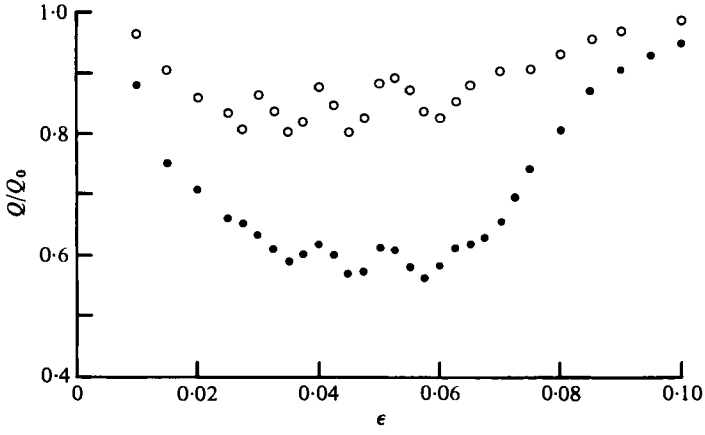

FIGURE 4. Dependence of Q/Q_0 on ϵ from fully nonlinear model with same parameters as figure 3. $h_0 = 0{\cdot}1$ (open circles), $h_0 = 0{\cdot}2$ (solid circles).

The results presented are for the parameter values $\beta = 0{\cdot}4$, $E^{\frac{1}{2}} = 0{\cdot}01$, $\theta_w = 0{\cdot}5$ and $h_0 = 0{\cdot}1, 0{\cdot}2$. (These can be re-scaled as described earlier. The choice $\beta = 0{\cdot}4, r_2 = 3$ corresponds to latitude circles 22° and 67° on a rotating sphere. Small $E^{\frac{1}{2}}$ is chosen to demonstrate resonance effects, and to explore the borderline between steady and unstable systems.) The response Q/Q_0 to varying forcing, as measured by $\epsilon\Omega_0$, is shown in figure 3. Several minima appear for westerly flow ($\Omega_0 = 1$). Their positions correspond to the first few resonance points predicted by the analytic theory for $n = 1$. (These are $\epsilon\Omega = \beta/\lambda_{m1}^2 = 0{\cdot}078, 0{\cdot}059, 0{\cdot}042, 0{\cdot}030, 0{\cdot}022, 0{\cdot}017$ for $m = 1$ to 6). The [flux] contribution to Q is found to be non-zero but small, so higher radial modes are involved but play a minor role. Multiple solutions are predicted for some ranges of ϵ. In the next section these predictions are compared with fully nonlinear results.

Q/Q_0 was also calculated using the M-equation. Curves of the same shape but with smaller Q/Q_0 were obtained, the difference increasing as h_0 increased.

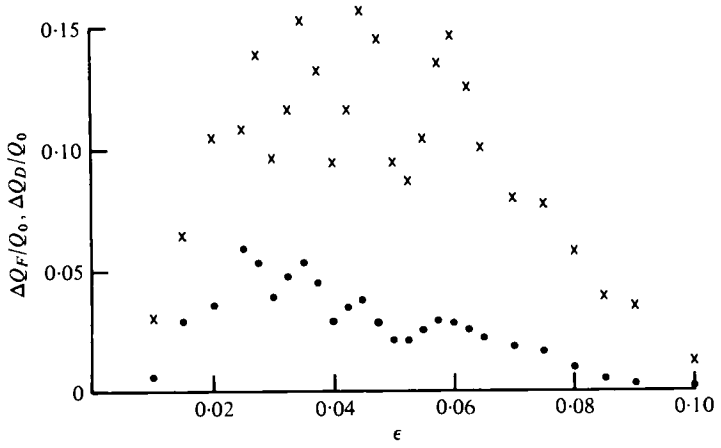

FIGURE 5. As for figure 4, showing $\Delta Q_F/Q_0$ (dots) and $\Delta Q_D/Q_0$ (crosses) for $h_0 = 0{\cdot}1$.

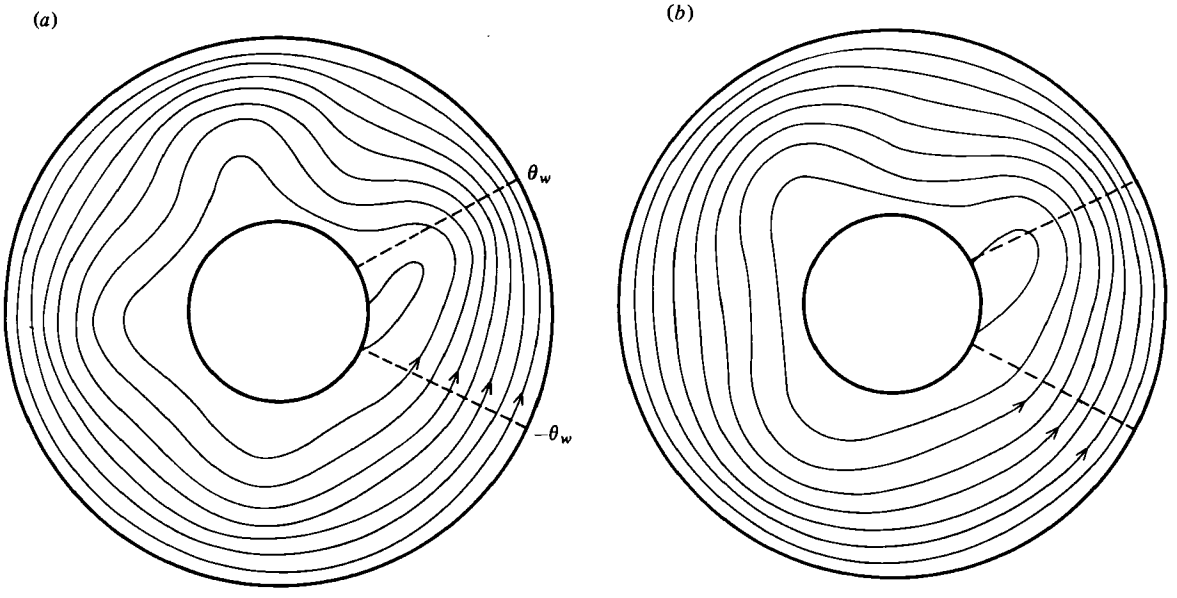

FIGURE 6(*a*, *b*). For legend see facing page.

4. Nonlinear results

Steady solutions of the fully nonlinear equations were obtained by spinning up the system with constant forcing from some initial conditions. Figure 4 shows the variation of Q/Q_0 with ϵ using the same parameters and topography as for figure 3. A series of minima appear, as expected, but the predicted multiple equilibria are not found. The simple implicit theory predicts the resonance positions reasonably well for small h_0, but in contrast to figure 3 the peaks in figure 4 do not shift and accentuate as h_0 is increased. Some of this discrepancy can be accounted for by using an improved theory, as described in the next section.

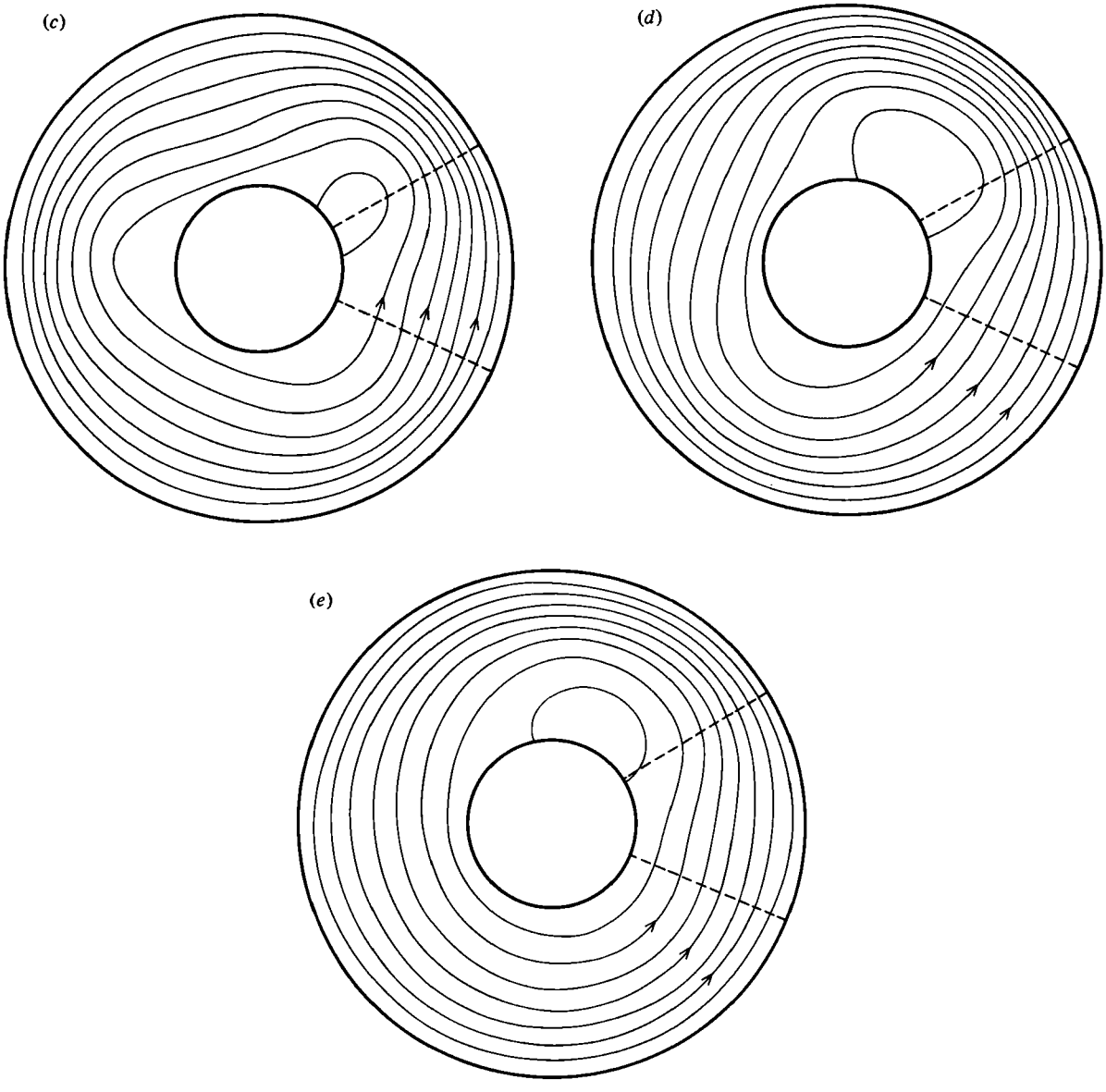

FIGURE 6. Streamlines (contours of ψ) from fully nonlinear model with $\beta = 0{\cdot}4$, $E^{\frac{1}{2}} = 0{\cdot}01$, $h_0 = 0{\cdot}1$. (*a*) $\epsilon = 0{\cdot}03$, (*b*) $\epsilon = 0{\cdot}04$, (*c*) $\epsilon = 0{\cdot}05$, (*d*) $\epsilon = 0{\cdot}06$, (*e*) $\epsilon = 0{\cdot}07$.

The change in Q can be separated into two parts:

$$\Delta Q_F = E^{-\frac{1}{2}} \int_{r_1}^{r_2} r^{-1}[\text{flux}]\, dr. \tag{4.1a}$$

and

$$\Delta Q_D = E^{-\frac{1}{2}} \int_{r_1}^{r_2} r^{-1}[\text{drag}]\, dr. \tag{4.1b}$$

$\Delta Q_F/Q_0$ and $\Delta Q_D/Q_0$ are plotted as functions of ϵ in figure 5, for $h_0 = 0{\cdot}1$. Both terms are always positive, with ΔQ_D larger but not always dominant. Note that $\Delta Q_F/\Delta Q_D$

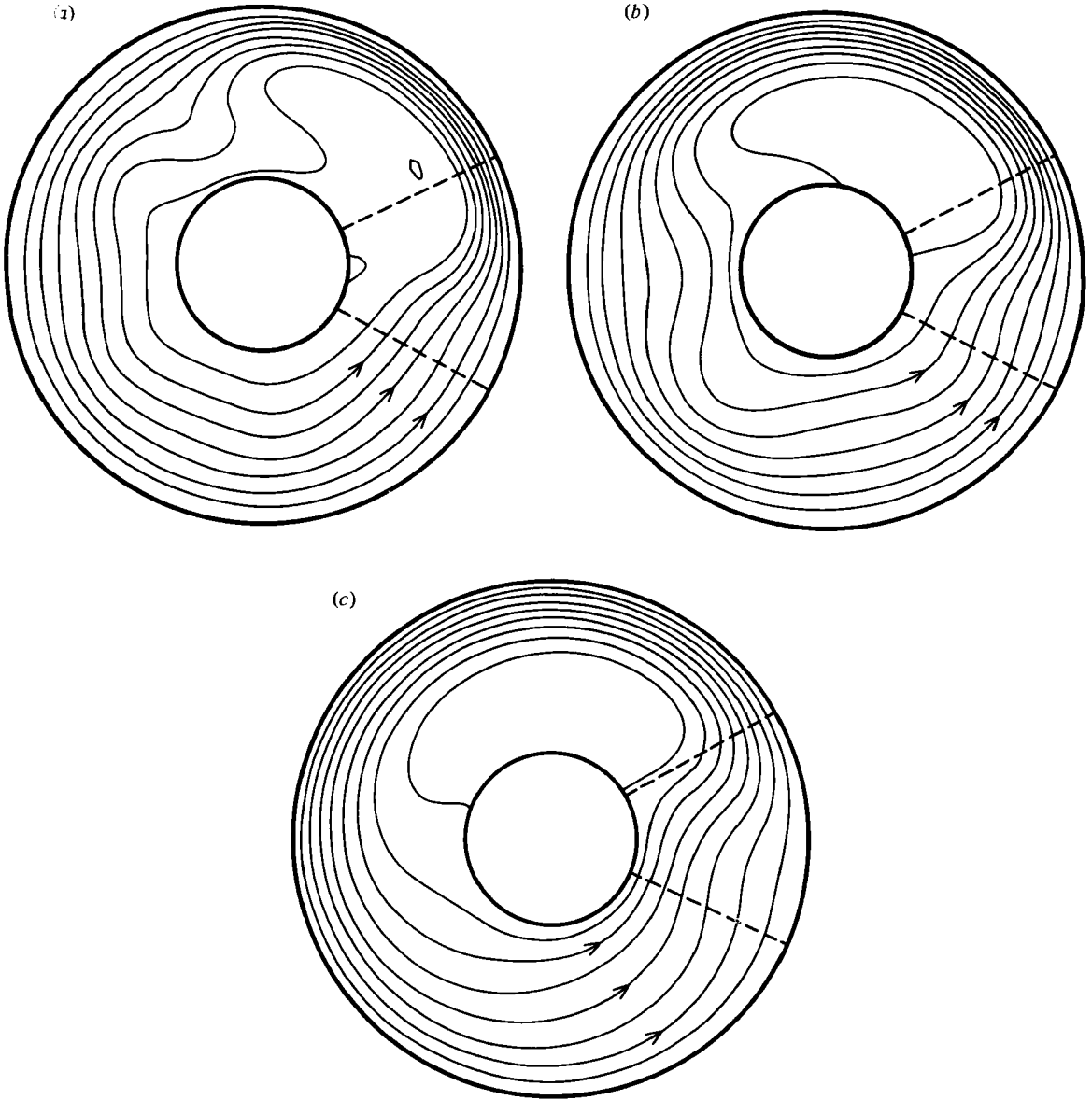

FIGURE 7. As for figure 6, with $h_0 = 0{\cdot}2$. (*a*) $\epsilon = 0{\cdot}03$, (*b*) $\epsilon = 0{\cdot}05$, (*c*) $\epsilon = 0{\cdot}07$.

does not scale like ϵ/h_0. For the example shown, ΔQ_F actually becomes less important as ϵ increases.

Flow patterns for several values of ϵ are given in figure 6, for $h_0 = 0{\cdot}1$. The wave-like perturbations extend right around the annulus. The decrease in zonal wavenumber as ϵ increases is clear. Relative to the zonal mean the perturbations are largest near the inner sidewall, as indicated by the closed gyres found in that region. As ϵ is increased beyond the resonant range ($\epsilon \gtrsim 0{\cdot}07$) the disturbance diminishes and the closed gyre is shifted further downstream from the obstacle. When the topography height is doubled the different zonal wavenumbers are less obvious and the system

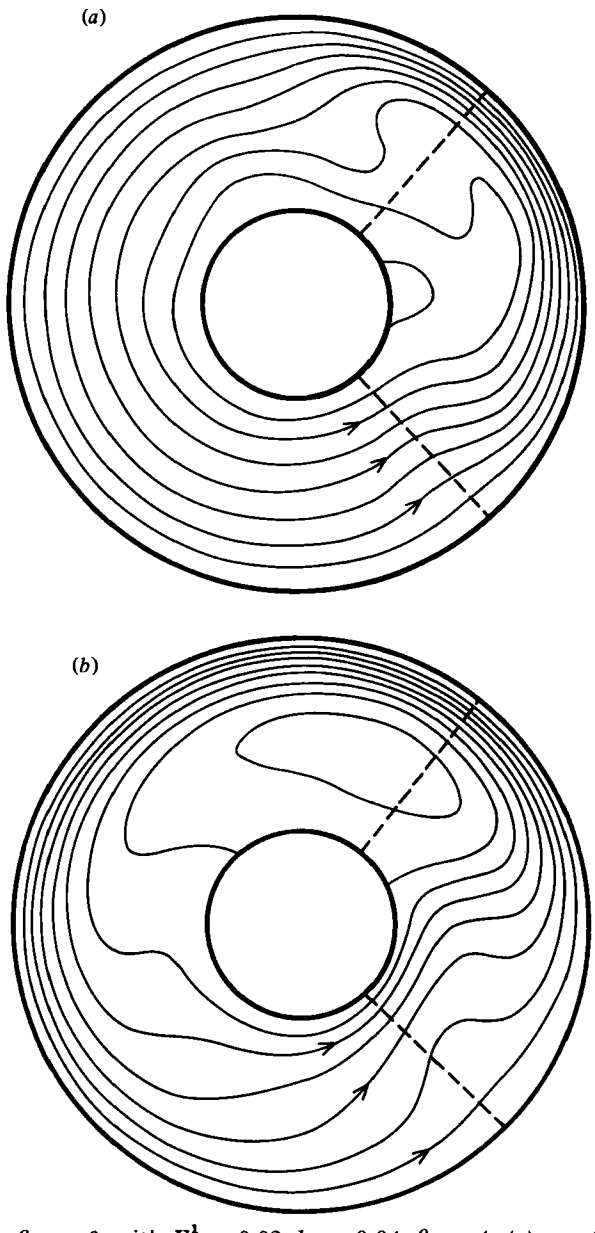

FIGURE 8. As for figure 6, with $E^{\frac{1}{2}} = 0{\cdot}02$, $h_0 = 0{\cdot}04$, $\theta_w = 1$. (*a*) $\epsilon = 0{\cdot}02$, (*b*) $\epsilon = 0{\cdot}06$.

is dominated by a large trough, as can be seen in figure 7. This behaviour is reflected in the coalescence of resonant points as h_0 increases, as explained in part 1.

Figure 8 shows the effect of doubling the dissipation parameter $E^{\frac{1}{2}}$. Even though the topography height and width are also doubled, so large deviations are caused, the disturbance is local rather than global in character. The vorticity change induced by a change in latitude or topographic stretching is forgotten before a parcel of fluid can travel far around the annulus, so resonance effects are not important. Corresponding radial profiles for $[v - v_0]$, and the [flux] and [drag] components, are shown in figure 9.

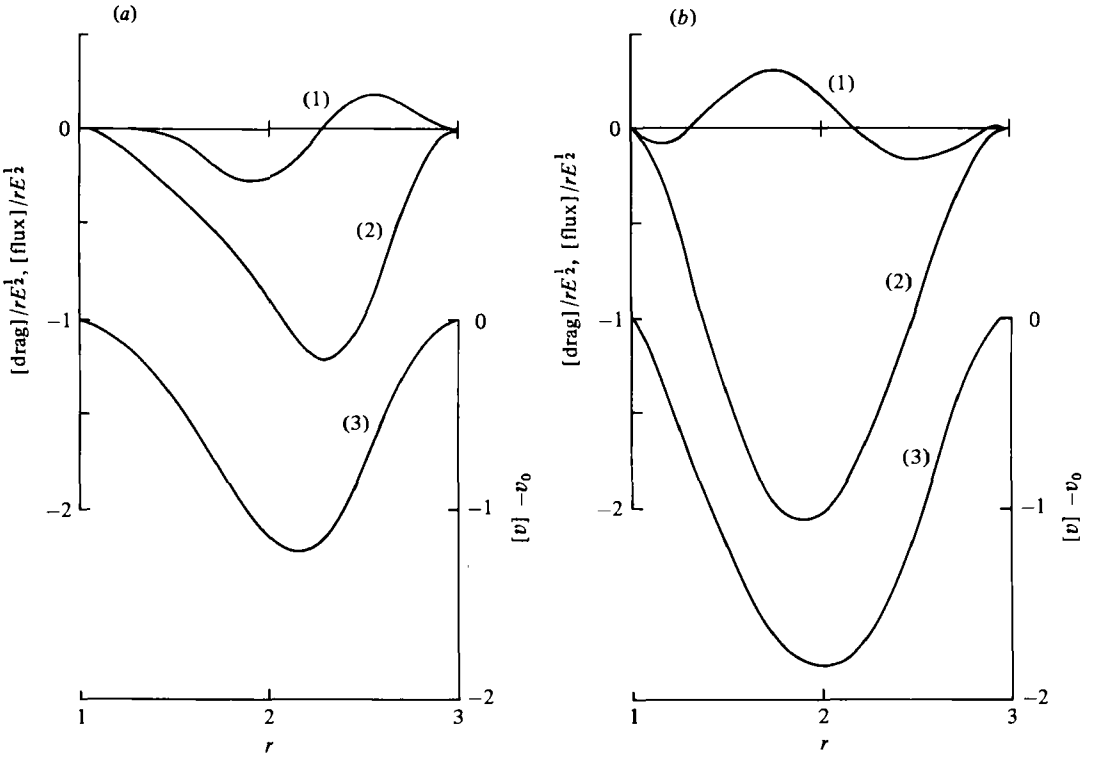

FIGURE 9. Radial profiles of (1) [flux]/$rE^{\frac{1}{2}}$, (2) [drag]/$rE^{\frac{1}{2}}$, (3) $[v-v_0]$, for the flows shown in figure 8. (*a*) $\epsilon = 0{\cdot}02$, (*b*) $\epsilon = 0{\cdot}06$.

The [drag] is everywhere negative with a minimum somewhat off-centre. The [flux] term is much smaller and changes sign, and compensates the [drag] such that the $[v-v_0]$ minimum is more central than that due to [drag] alone. The [flux] and [drag] profiles change as ϵ changes and a consistent approximation of them is not obvious. The $[v-v_0]$ profile is less sensitive however, and can be usefully parametrized.

5. Improved quasi-linear model

The profiles for $[v-v_0]$ given in the previous section suggest the approximation

$$[v-v_0] = -CP^2(r) = -C\sin^2\pi\left(\frac{r-r_1}{r_2-r_1}\right). \tag{5.1}$$

$P(r)$ is the radial topography profile, and the parameter C is related to Q by

$$C\int_{r_1}^{r_2} P^2(r)\,dr = Q_0 - Q. \tag{5.2}$$

This choice for $[v]$ satisfies the side-wall conditions $[v] = v_0$. It is supported by the analytic model of § 3, which gives $[v-v_0]$ proportional to $(R/r)^2$ for topography with one radial mode, and by the success of the same relation in part 1. Further, it seems physically reasonable to have the change in $[v]$ largest where the obstacle is highest.

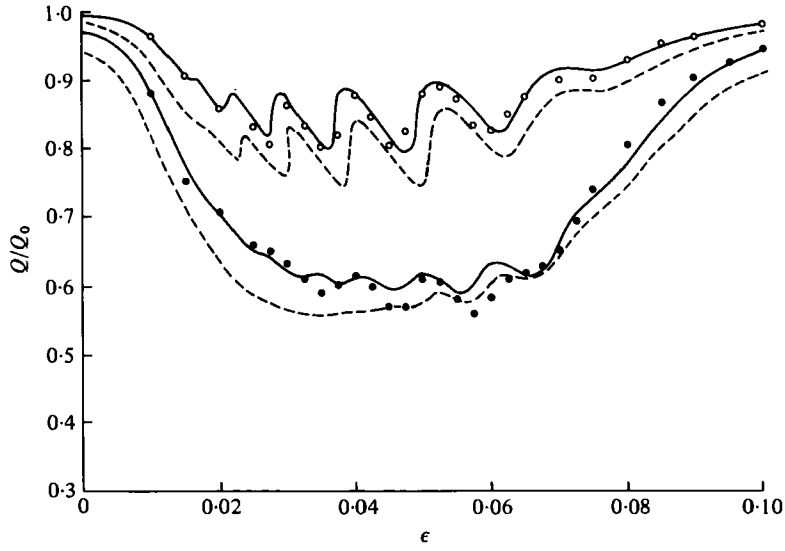

FIGURE 10. Dependence of Q/Q_0 on ϵ according to the improved implicit theory using the Q-equation (solid lines) and the M-equation (dashed lines). Parameters are the same as in figure 4, and the fully nonlinear results are repeated for comparison.

Note that in contrast to the simpler basic flow Ωr this new approximation has a non-zero vorticity gradient

$$[\zeta]_r = \tfrac{1}{2}C\left\{\frac{1}{r^2} - \frac{2\pi}{r(r_2-r_1)}\sin 2\pi\left(\frac{r-r_1}{r_2-r_1}\right) - \left(\frac{1}{r^2}+\frac{4\pi^2}{(r_2-r_1)^2}\right)\cos 2\pi\left(\frac{r-r_1}{r_2-r_1}\right)\right\}. \tag{5.3}$$

Given some value for C the corresponding eddy structure can be found from (3.10). The Q-equation then gives a new estimate for Q, and hence for C, and the process can be repeated. (In practice it is simpler to find h_0 for some estimate of C, then adjust C accordingly to iterate to the required h_0. It is also possible to iterate along lines of constant $\epsilon Q/Q_0$, which is useful for investigating multiple solution regimes.)

Figure 10 compares results obtained by this method with the nonlinear solutions shown in figure 4. There is good agreement for $h_0 = 0{\cdot}1$, with positions and magnitudes of minima corresponding quite well. The quasi-linear solutions somewhat overestimate the attenuation of resonant points for larger h_0, but are still satisfactorily close to the exact results. In contrast to the simpler model, no multiple equilibria are predicted. The use of a more realistic $[v]$ profile is a considerable improvement.

C is also related to M by

$$C\int_{r_1}^{r_2} r^2P^2(r)\,dr = M_0 - M,$$

and M is similarly related to Q, so quasi-linear solutions for Q/Q_0 can alternatively be obtained using the M-equation. These results are included in figure 10. In general the M-equation method underestimates Q/Q_0, particularly for small ϵ, and the Q-equation is preferable. For $h_0 = 0{\cdot}2$ and $\epsilon \simeq 0{\cdot}06$, however, there is little to choose between them.

Results for doubled dissipation and topography are given in figure 11, using the Q-equation. Again agreement is good, even for changes in Q/Q_0 of up to 50 %. As

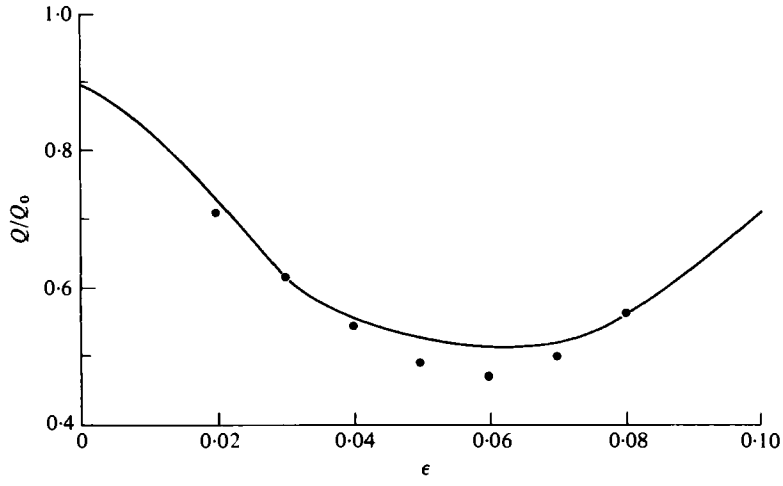

FIGURE 11. Dependence of Q/Q_0 on ϵ for fully nonlinear (circles) and improved implicit (solid line) models, with $\beta = 0{\cdot}4$, $E^{\frac{1}{2}} = 0{\cdot}2$, $h_0 = 0{\cdot}4$, $\theta_w = 1$.

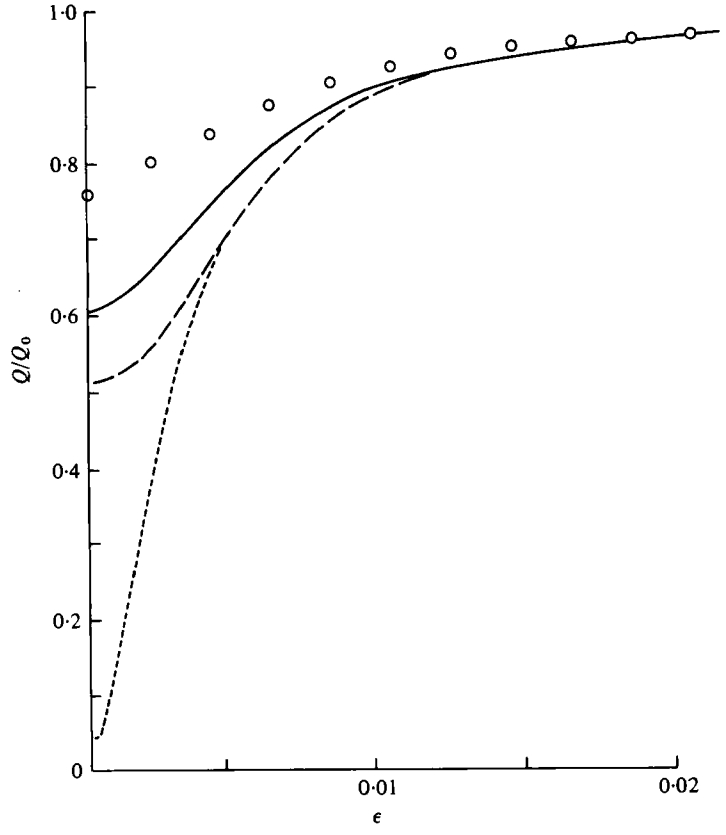

FIGURE 12. Dependence of Q/Q_0 on ϵ for fully nonlinear (circles), improved implicit (solid line), simple implicit (dashed line), and linear perturbation (dotted line) theories, for $\beta = 0$, $E^{\frac{1}{2}} = 0{\cdot}01$, $h_0 = 0{\cdot}1$, $\theta_w = 0{\cdot}5$.

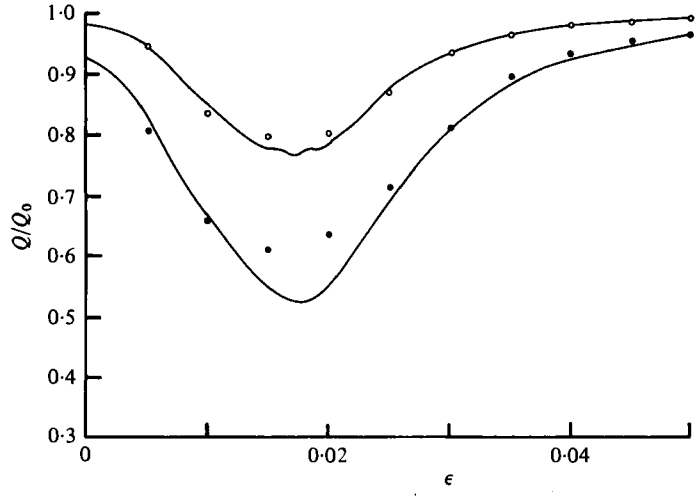

FIGURE 13. As for figure 10, with $r_2 = 2$ instead of 3.

expected for larger dissipation there is no sign of individual resonant waves, and a broad minimum is found instead.

For the case $\beta = 0$ a comparison of several models is given in figure 12. When $[v] = \Omega_0 r$ the implicit theory reduces to the linear perturbation method used by Davey (1978) for an f-plane annulus. This method greatly overestimates the decrease in Q/Q_0 as $\epsilon \to 0$. The simplest implicit technique gives an improved estimate, and the improved implicit method is better yet, but the topographic drag is still substantially overestimated for small ϵ. The difficulty is that when $\beta = 0$ the vorticity generated by $\mathbf{u} \cdot \nabla h$ cannot be balanced by $u\beta$, and must be balanced by friction effects alone as $\epsilon \to 0$. The solution then depends heavily on the representation of $\mathbf{u} \cdot \nabla h$, particularly when $E^{\frac{1}{2}}$ is small.

6. The effect of varying the annulus width

The non-dimensional inner radius is $r_1 = 1$, by definition. Changing the outer radius r_2 is equivalent to changing the latitude range on a sphere, and this effect is explored in this section. For the results given β is not changed as r_2 varies, so the equivalent central latitude also varies slightly. This effect can be compensated by rescaling the other external parameters. Details and tables of latitudes are given in appendix C.

Fully nonlinear and quasi-linear results for Q/Q_0 are given in figures 13 and 14 for $r_2 = 2$ and 4, and should be compared with figure 10. When r_2 is reduced from 3 to 2 (figure 13) resonant effects are greatly reduced. The decrease in meridional length scale increases the wavenumbers for free Rossby waves, which effectively increases their dissipation rate. (Analytically, the eigenvalues λ^2 described in appendix A increase as r_2 decreases. Resonant values of ϵ decrease correspondingly, as can be seen from the changes in scales for ϵ in figures 10, 13, and 14.) The quasi-linear approximation is good for $h_0 = 0{\cdot}1$, but overestimates the maximum change in Q as h_0 increases.

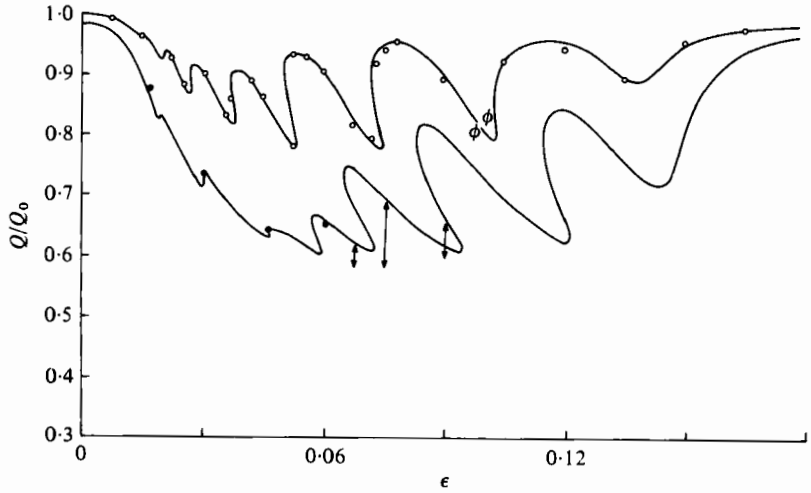

FIGURE 14. As for figure 10, with $r_2 = 4$ instead of 3.

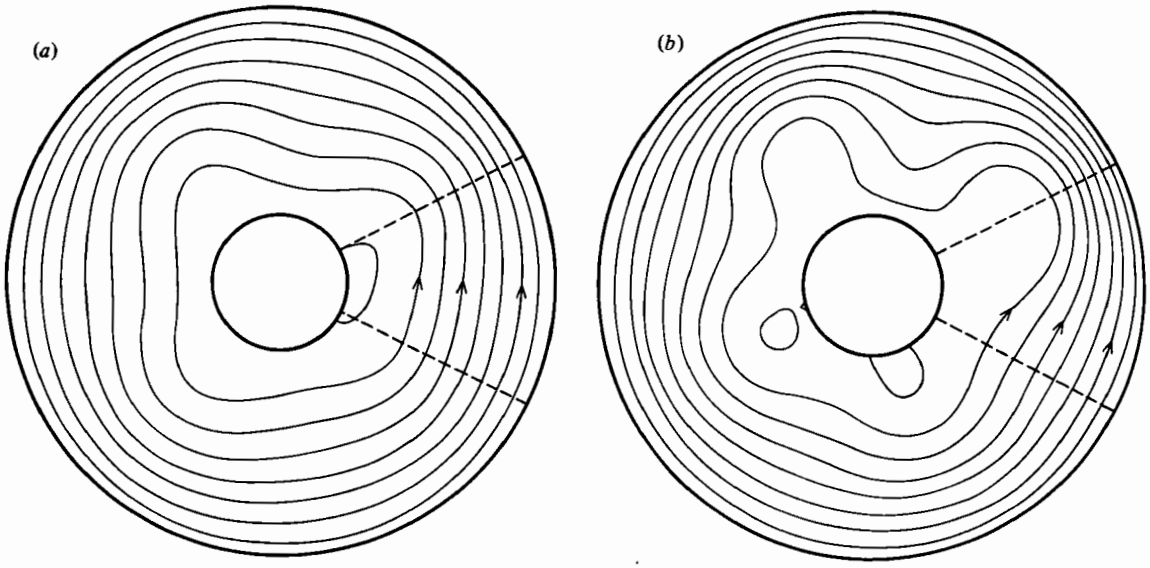

FIGURE 15. Alternative stable states from the fully nonlinear model with $r_2 = 4$, $\beta = 0{\cdot}4$, $E^{\frac{1}{2}} = 0{\cdot}01$, $h_0 = 0{\cdot}1$, $\epsilon = 0{\cdot}052$. (*a*) High index state, $Q/Q_0 = 0{\cdot}93$; (*b*) low index state, $Q/Q_0 = 0{\cdot}78$.

Increasing r_2 to 4 (figure 14) has the opposite effect of enhancing the resonance effects. Multiple solutions are now predicted by the improved quasi-linear theory, and increasing h_0 at first increases rather than decreases the predicted multiplicity regime. For $h_0 = 0{\cdot}1$ the predicted behaviour is largely confirmed by the nonlinear results. Multiple equilibria are found at $\epsilon = 0{\cdot}052$, with zonal wavenumber 4 dominating. Flow patterns for the alternative steady states are given in figure 15. An initial state

$(u, v) = (0, v_0)$ leads to a strongly zonal flow (figure 15*a*) with $Q/Q_0 = 0{\cdot}93$, whereas a system initially at rest evolves to the pattern shown in figure 15*b* with $Q/Q_0 = 0{\cdot}78$ and prominent wavenumber 4.

Other multiple regions predicted for $h_0 = 0{\cdot}1$ were not verified. For zonal wavenumber 3 solutions were found that evolved very slowly, and for $m = 2$ regular small amplitude oscillations developed. (The amplitude is indicated in figure 14, and the period is about 10 'days'.) At the larger values of ϵ associated with these resonant modes the system is barotropically unstable for large perturbations. Hart (1979) and Charney & DeVore (1979) have discussed this effect in more detail; it involves an exchange of energy between eddies and mean flow via eddy–topography interactions.

For $h_0 = 0{\cdot}2$ the nonlinear and quasi-linear results agree for small ϵ, but as ϵ increases irregular and slowly developing oscillations appear in the nonlinear system. (The ranges of some such fluctuations are given in figure 14.) The steady quasi-linear model is then useful only as a rough indicator of the average Q to expect.

The quasi-linear model was also solved with r_2 and β varied to simulate expansion of meridional scale about some constant central latitude. Results similar to those already described were obtained as r_2 varied.

7. Summary and applications

In part 1 quasi-linear models of steady flow over topography in a periodic channel were presented. A similar hierarchy has been developed for an annular system in an effort to bridge the gap between channel and spherical geometry, and also to produce results more amenable to experimental verification.

The results are basically the same as part 1. The dynamics involves a balance of topographic generation and relative advection of Rossby waves, with small dissipation. For westerly flow resonances can create large perturbations, with correspondingly reduced zonally averaged flow. Conditions for resonance can be estimated analytically using a uniform zonal flow profile. The Rossby-wave properties depend on the $[v]$ profile however, and results were greatly improved by using a more realistic $[v]$ related to the topography shape.

The resulting improved implicit model is much simpler than a nonlinear one, and can be used to anticipate the behaviour of a system for a wide range of parameters. Predictions are generally in good agreement with exact nonlinear results, so the neglect of eddy interactions in the eddy vorticity equation is justified. The limits of validity seem to be indicated by the onset of multiple solutions. For relatively small h_0 and ϵ the nonlinear system has multiple states as predicted. For larger values however oscillatory or irregular fluctuations develop through barotropic instability, and the steady quasi-linear approximation no longer applies.

The main application of this theory is to the dynamics of large-scale perturbations in the atmosphere. (The emphasis is on dynamical descriptions of phenomena rather than quantitative calculations.) For large-scale forcing the response of the atmosphere typically has a similar pattern at all heights, so a barotropic model can be used as a first approximation. The β-plane annulus represents a region between latitudes where flow is dominantly zonal. The topography used in the theory can also be interpreted as forcing by diabatic heating. (Note that the effective h_0 is smaller than its physical value because flow in the atmosphere is slower than average near ground level.) The

basic zonal flow is forced by some unspecified mechanism, but is ultimately related to the equator–pole temperature gradient.

A realistic relaxation time is about 10 days, which corresponds to $E^{\frac{1}{2}} = 0{\cdot}01$. This is the value used in most of the results described earlier. (The results given for $E^{\frac{1}{2}} = 0{\cdot}02$ can be reinterpreted for $E^{\frac{1}{2}} = 0{\cdot}01$ by halving the associated values of ϵ, β and h_0.)

For a large latitude range ($r_2 = 4$) the response of the system is very sensitive to h_0 and ϵ for $0{\cdot}03 \lesssim \epsilon \lesssim 0{\cdot}1$. ($\epsilon = 0{\cdot}05$ corresponds to a circulation time of 10 days in the absence of perturbations, so in practice $\epsilon \lesssim 0{\cdot}05$.) Small changes in forcing can cause major changes in the character of the flow. There may be a switch between low and high index stable states, like those shown in figure 15, or perhaps a change from stable to fluctuating conditions. These calculations show that the feedback mechanisms described in part 1, and extended in this paper, may play an important role in the dynamics of atmospheric phenomena such as large-scale blocking.

For smaller latitude ranges the system is less sensitive. Multiple equilibria are not found, though their occurrence cannot be ruled out because the theory contains many approximations. (For example, the basic zonal flow and the topography are not realistic, and baroclinic effects are ignored.) Changes in ϵ can still cause large changes in flow patterns, however, as seen in figure 6. The system is sensitive to changes in internal Rossby number $\epsilon Q/Q_0$ as well as ϵ, so internal fluctuations as well as external driving changes can alter the flow.

It is interesting to compare analytic resonance conditions for the channel and annular geometry. For $r_2 = 3$ and $\beta = 0{\cdot}4$, zonal wavenumbers 1, 2, 3, 4 are resonant ($\epsilon\Omega = \beta/\lambda^2$) for wind speeds of 39, 29, 21, and 15 m/sec respectively, at latitude 45°. A channel of length $L^* = 2\pi R^* \sin\phi_A$ and breadth $R^*(\phi_2 - \phi_1)$ has corresponding resonant wind speeds of 35, 26, 19, and 13 m/sec, almost the same. The difference between channel and annulus models is more evident in the flow patterns. Perturbations in the annulus are asymmetric with respect to latitude, being relatively larger at higher latitudes.

Another difference between channel and annulus theories is the effect of meridional eddy vorticity flux on Q. For the cases investigated, this [flux] augments the net topographic [drag]. The topography used effectively had only one radial mode however, so this effect was slight.

The relevance of the theory to ocean currents is less direct. For planetary scales the oceanic Rossby number is much smaller than its atmospheric counterpart. Vorticity advection is negligible, and global Rossby-wave effects are not significant. Dissipation is also small, and in relatively weakly stratified regions such as the Southern Ocean currents tend to follow the large-scale contours of f/H. Kamenkovich (1962) and Johnson & Hill (1975) have made use of this property to estimate topographic influence on the steady zonal transport by the Antarctic Circumpolar Current (A.C.C.). As mentioned in part 1, however, the eddy–topography mean flow interactions described by the quasi-linear theory may be important locally on intermediate scales. These smaller scales can in turn influence the large-scale mean circulation. For large length and topography height scales currents go around rather than over obstacles and there is a low correlation between ϕ and h_θ. This constraint is less severe for smaller obstacles and shorter length scales, so the [drag] due to a medium size hill may be as important as that of a large ridge. Further, the pattern of flow over a moderate obstacle is more sensitive to changes in the driving force than is the flow around a large one, so variations in the overall [drag] may well be determined by the medium scale dynamics.

The hybrid of planetary f/H flow and quasi-linear theory required to test this hypothesis is beyond the scope of this paper, but would help resolve the question of the relative effects of a few large ridges and a field of smaller hills. Such a model would have direct application to the dynamics of the A.C.C., for which large fluctuations in the net circumpolar transport have been observed.

Investigation of the M-equation and the effect of varying annulus width was made at the suggestion of the referees. The semi-spectral numerical model was developed while the author was visiting the National Centre for Atmospheric Research, which is sponsored by the National Science Foundation.

Appendix A. Orthogonal radial modes and Rossby waves

The equation for the radial eigenfunctions $R(r)$ is

$$r\frac{d}{dr}\left(r\frac{dR}{dr}\right)-m^2R+\lambda^2rR=0, \tag{A 1}$$

with boundary conditions $R(r_1)=R(r_2)=0$. The change of variable $4\lambda^2r=x^2$ leads to Bessel's equation. This gives

$$R(r)=J_{2m}(x_1r^{\frac{1}{2}}/r_1^{\frac{1}{2}})\,Y_{2m}(x_1)-Y_{2m}(x_1r^{\frac{1}{2}}/r_1^{\frac{1}{2}})\,J_{2m}(x_1) \tag{A 2}$$

where $x_1^2=4\lambda^2r_1$ and J_{2m}, Y_{2m} are Bessel functions of the first and second kind. The parameter x_1, and hence λ^2, is determined by the requirement $R(r_2)=0$. The eigenvalues λ_{mn}^2, corresponding to the nth zero of (A 2) for wavenumber m, can thus be calculated. The first few values for $r_1=1$, $r_2=3$ are given in table 1.

The orthogonality relation for these radial modes is

$$\int_{r_1}^{r_2}R_mR_n\,dr=0,\quad m\neq n. \tag{A 3}$$

The free inviscid Rossby wave

$$\phi=R(r)\,e^{im(\theta-ct)}$$

is a solution of

$$\omega\nabla^2\phi_t+\frac{1}{r}\beta\phi_\theta=0$$

if the angular wave speed is $c=\beta/\omega\lambda^2$. In particular, a free standing Rossby wave can exist in the uniform flow $v=\Omega r$ when

$$\epsilon\Omega=\beta/\lambda^2. \tag{A 4}$$

Appendix B. Fully nonlinear numerical model

A mixture of spectral and finite-difference methods was used to construct a fully nonlinear numerical model. The stream function is written as

$$\psi=[\psi]+\Sigma A_m(r,t)\cos m\theta+B_m(r,t)\sin m\theta, \tag{B 1}$$

with $A_m = B_m = 0$ on side walls. The topography is represented by

$$h = h_0 \Sigma f_m(r) \cos m\theta + g_m(r) \sin m\theta, \tag{B 2}$$

with $f_m = g_m = 0$ on side walls for simplicity.

The radial finite-difference calculations required are simplified by the transformation

$$r = r_2 e^{-y}. \tag{B 3}$$

Then, for example,

$$r^2 J(\psi, \chi) = \psi_\theta \chi_y - \psi_y \chi_\theta.$$

With a uniform y-grid this transformation has the additional advantage of having the r-grid spacing smallest near the inner sidewall, where the flow is most sensitive to perturbations.

For conservation of energy and enstrophy when the flow is inviscid the Jacobians must be rewritten as

$$\begin{aligned} r^2 J(\psi, \chi) &= \tfrac{1}{3}\{\psi_\theta \chi_y - \psi_y \chi_\theta + (\psi_\theta \chi)_y - (\psi_y \chi)_\theta \\ &\quad + (\psi \chi_y)_\theta - (\psi \chi_\theta)_y\} \\ &= \mathscr{J}(\psi, \chi). \end{aligned} \tag{B 4}$$

With trapezoidal integration and differentiation in the form $\psi_{yi} = (\psi_{i+1} - \psi_{i-1})/\Delta y$, the usual rules for integration by parts can be used to verify the conservation constraints.

The vorticity is written as

$$r^2 \nabla^2 \psi = W + \Sigma\, WA_m \cos m\theta + WB_m \sin m\theta \tag{B 5}$$

where

$$W = [\psi]_{yy} - m^2[\psi], \quad WA = A_{yy} - m^2 A, \quad WB = B_{yy} - m^2 B. \tag{B 6}$$

The quasi-geostrophic vorticity equation gives

$$\omega W_t = E^{\frac{1}{2}}(2\Omega_0 r^2 - W) - [\mathscr{J}(\phi, \epsilon \nabla^2 \phi + h)], \tag{B 7a}$$

$$\begin{aligned} \tfrac{1}{2}\omega WA_t = &-\tfrac{1}{2}E^{\frac{1}{2}} WA - [\cos m\theta \{\mathscr{J}([\psi], \epsilon \nabla^2 \phi + h) \\ &+ \mathscr{J}(\phi, \epsilon [\psi]_{yy} + \beta r + \epsilon \nabla^2 \phi + h\}], \end{aligned} \tag{B 7b}$$

$$\begin{aligned} \tfrac{1}{2}\omega WB_t = &-\tfrac{1}{2}E^{\frac{1}{2}} WB - [\sin m\theta \{\mathscr{J}([\psi], \epsilon \nabla^2 \phi + h) \\ &+ \mathscr{J}(\phi, \epsilon [\psi]_{yy} - \beta r + \epsilon \nabla^2 \phi + h\}]. \end{aligned} \tag{B 7c}$$

W, WA_m and WB_m are found by time stepping from some initial conditions. The stream function at each time step is obtained by solving (B 6). The sidewall conditions required to find $[\psi]$ are found from the transport equation and circulation constraints.

Advantages of the semi-spectral scheme are that the radial finite-difference equations can be rapidly solved by tridiagonal matrix methods, and that only azimuthal spectral interaction coefficients are needed. (Further, these coefficients are ± 1, so need not be stored.) This is particularly suitable for low resolution numerical experiments. Typically 10 to 15 zonal modes and about 30 radial grid points were adequate for the experiments described.

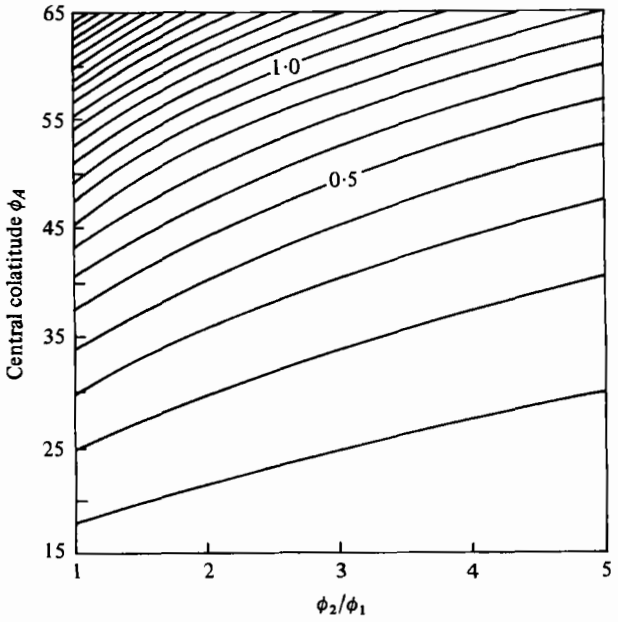

FIGURE 16. Contours of $\beta = 2\phi_A \tan \phi_A/(1+\phi_2/\phi_1)$.

Appendix C. Relation between spherical, annulus, and channel geometry

Suppose a sphere has radius R^* and rotation rate Ω^*, and we wish to approximate the region between co-latitudes ϕ_1 and ϕ_2 by a β-plane annulus. The appropriate radii are $r_1^* = R^*\phi_1$ and $r_2^* = R^*\phi_2$. The β-plane approximation gives

$$f^* = f_A^* - \beta^*(r^* - r_A^*),$$

where

$$f_A^* = 2\Omega^* \cos\phi_A, \quad \beta^* = 2\Omega^* \sin\phi_A/R^*,$$
$$r_A^* = R^*\phi_A = R^*(\phi_1+\phi_2)/2.$$

With length scale r_1^* we find

$$f = 1 - \beta(r - r_A)$$

with

$$\beta = \beta^* r_1^*/f_A^* = \phi_1 \tan\phi_A = 2\phi_A \tan\phi_A/(1+\phi_2/\phi_1).$$

Figure 16 gives contours of β for varying ϕ_2/ϕ_1 and ϕ_A, and is useful for rescaling the external parameters. For example, table 2*a* shows co-latitudes associated with $\beta = 0{\cdot}4$, $\phi_2/\phi_1 = 2, 3, 4$. If $\omega, E^{\frac{1}{2}}, \beta, \epsilon, h_0$ are halved, the same solutions of the quasi-geostrophic equations apply to the co-latitudes given in table 2*b* for $\beta = 0{\cdot}2$.

To approximate the same region by a β-plane channel, the relevant length and breadth is

$$l^* = 2\pi R^* \sin\phi_A, \quad b^* = R^*(\phi_2 - \phi_1).$$

If length scale $L^* = R^* \sin\phi_A$ is chosen (as in part 1), then corresponding non-dimensional terms are

$$l = 2\pi, \quad b = (\phi_2 - \phi_1)/\sin\phi_A.$$

	$m = 1$	2	3	4	5	6
$n = 1$	5·12	6·76	9·47	13·2	17·9	23·4
2	19·0	20·7	23·5	27·5	32·7	39·1
3	42·0	43·7	46·6	50·6	55·8	62·3

TABLE 1. Eigenvalues λ^2_{mn}

	ϕ_2/ϕ_1				ϕ_2/ϕ_1	
(a) $\beta = 0{\cdot}4$	2	3	4	(b) $\beta = 0{\cdot}2$	2	3	4
ϕ_A	40·4	45·3	49·3	ϕ_A	29·9	34·0	37·4
ϕ_1	26·9	22·7	19·7	ϕ_1	19·9	17·0	15·0
ϕ_2	53·9	68·0	78·9	ϕ_2	39·9	51·0	59·9

TABLE 2. Co-latitudes for various values of β and $\phi_2/\phi_1 = r_2/r_1$

The parameter for the β-effect, as defined in part 1, is

$$\hat{\beta} = \beta^* L^*/f_A^* = \sin\phi_A \tan\phi_A.$$

For example, $\phi_A = 45°$ and $\phi_2/\phi_1 = 3$ requires $b = 1{\cdot}1$ and $\hat{\beta} = 0{\cdot}7$ for the channel approximation.

REFERENCES

CHARNEY, J. G. & DEVORE, J. G. 1979 Multiple flow equilibria in the atmosphere and blocking. *J. Atmos. Sci.* **36**, 1205–1216.

DAVEY, M. K. 1978 Recycling flow over bottom topography in a rotating annulus. *J. Fluid Mech.* **87**, 497-520.

DAVEY, M. K. 1980 A quasi-linear theory for rotating flow over topography. Part 1: Steady β-plane channel. *J. Fluid Mech.* **99**, 267–292.

FRENZEN, P. 1955 Westerly flow past an obstacle in a rotating hemispherical shell. *Bull. Am. Met. Soc.* **36**, 204–210.

FULTZ, D. & FRENZEN, P. 1955 A note on certain interesting ageostrophic motions in a rotating hemispherical shell. *J. Met.* **12**, 332–338.

FULTZ, D. & LONG, R. R. 1951 Two-dimensional flow around a circular barrier in a rotating spherical shell. *Tellus* **3**, 61–68.

HART, J. E. 1979 Barotropic quasi-geostrophic flow over anisotropic mountains. *J. Atmos. Sci.* **36**, 1736–1746.

HAURWITZ, B. 1940*a* The motion of atmospheric disturbances. *J. Mar. Res.* **3**, 35–50.

HAURWITZ, B. 1940*b* The motion of atmospheric disturbances on the spherical earth. *J. Mar. Res.* **3**, 254–267.

HOLTON, J. R. 1971 An experimental study of forced barotropic Rossby waves. *Geophys. Fluid Dyn.* **2**, 323–341.

JOHNSON, J. A. & HILL, R. B. 1975 A three-dimensional model of the Southern Ocean with bottom topography. *Deep-Sea Res.* **22**, 745–752.

KAMENKOVICH, V. M. 1962 On the theory of the Antarctic Circumpolar Current. *Akad. Nauk. S.S.R. Inst. Okean. Trudy* **56**, 241–293.

LONG, R. R. 1952 The flow of a liquid past a barrier in a rotating spherical shell. *J. Met.* **9**, 187–199.

PHILLIPS, N. A. 1965 Elementary Rossby waves. *Tellus* **17**, 295–301.